Measurement 222 (2023) 113644

Contents lists available at ScienceDirect

Measurement

journal homepage: www.elsevier.com/locate/measurement

Advances on the detection and measurement of bubble contours during subcooled boiling in microgravity

Xenophon Zabulis [a,*], Polykarpos Karamaounas [a], Ourania Oikonomidou [b], Sotiris Evgenidis [b], Margaritis Kostoglou [b], Martin Schinnerl [c], Axel Sielaff [c], Peter Stephan [c], Thodoris Karapantsios [b]

[a] Institute of Computer Science, Foundation for Research and Technology - Hellas, N. Plastira 100 Vassilika Vouton, Heraklion, 70013, Crete, Greece
[b] Laboratory of Chemical and Environmental Technology, School of Chemistry, Aristotle University of Thessaloniki, University Campus, Thessaloniki, 54124, Greece
[c] Institute for Technical Thermodynamics, Technische Universität Darmstadt, Alarich-Weiss-Str. 10, Darmstadt, 64287, Germany

ARTICLE INFO

MSC:
62H35
76Txx

Keywords:
Multi-phase imaging
Bubble detection
Subcooled boiling
Boiling
Microgravity
Image processing

ABSTRACT

A method for the detection of bubble contours in images of subcooled boiling in microgravity is proposed. The method refines an initial, rough contour approximation obtained from conventional background subtraction. This refinement entails the warping of an elliptical ring image region into a polar image, where bubble contour detection becomes simpler. The proposed method exhibits robustness to a wide variety of visual phenomena that typically hinder the detection of bubble contours. This is achieved by the grouping of continuous image edges. A ground truth annotated data set is provided that enables the quantitative and comparative evaluation of the proposed methods.

1. Introduction

The study of boiling phenomena is complex because it involves the combined action of heat and mass transport, which depend on multiple factors. The measurement of bubble size and shape is important for investigating the underlying physical phenomena. This work pertains to the domain of subcooled boiling, where the liquid bulk average temperature is less than the saturation temperature and, thus, a phase change occurs only on the walls of the heated substrate.

The study of multiphase phenomena is aided by image processing methods, operating on high-speed video recordings of those [1,2]. This work studies the special case of subcooled boiling in microgravity, following the reference in [1], where it is explained how measurements in microgravity aid the understanding of boiling in general. Pertaining to this work is that the absence of buoyancy leads to different bubble formations than already studied in terrestrial experiments (e.g., [3–5]). The dominant difference is the continuous bubble growth instead of detachment from the substrate. Another difference is brought by the growth of bubble size, which gives rise to practical inconveniences, such as the occurrence of the bubble in low-contrast areas or the reflections of other bubbles.

1.1. Challenges

Image analysis in boiling conditions is challenging as multiple phenomena occur rapidly and simultaneously. This work provides a method to study bubble growth in microgravity for varying experimental conditions, including pressure, heat flux, and subcooling temperature, through high-speed video. These conditions give rise to challenging artifacts inter-bubble reflections and lack of contrast. As such artifacts are present in other, more general bubble measurement problems, e.g. [3,4,6], their treatment by this work can contribute to other types of bubble measurements.

Some works simplify contour tracing, by carefully configuring the imaging apparatus. The working principle is to configure the imaging conditions to guarantee high contrast between the bubble and the background. This way, edges provide reliable boundary localization tools. Background subtraction and edge detection methods can then be used to trace bubble contours in images, e.g. [7–10]. However, this principle is hard to reach because our scene involves multiple interacting bubbles, giving rise to complex illumination artifacts, inter-, and intra-bubble reflections, as well as minute or zero image contrast. Moreover, due to boiling, these phenomena include evaporation, viscous flow, and non-equilibrium effects near the vapor–liquid interface that give rise to additional artifacts and noise [1].

* Corresponding author.
E-mail address: zabulis@ics.forth.gr (X. Zabulis).

https://doi.org/10.1016/j.measurement.2023.113644
Received 18 February 2023; Received in revised form 17 August 2023; Accepted 29 September 2023
Available online 11 October 2023

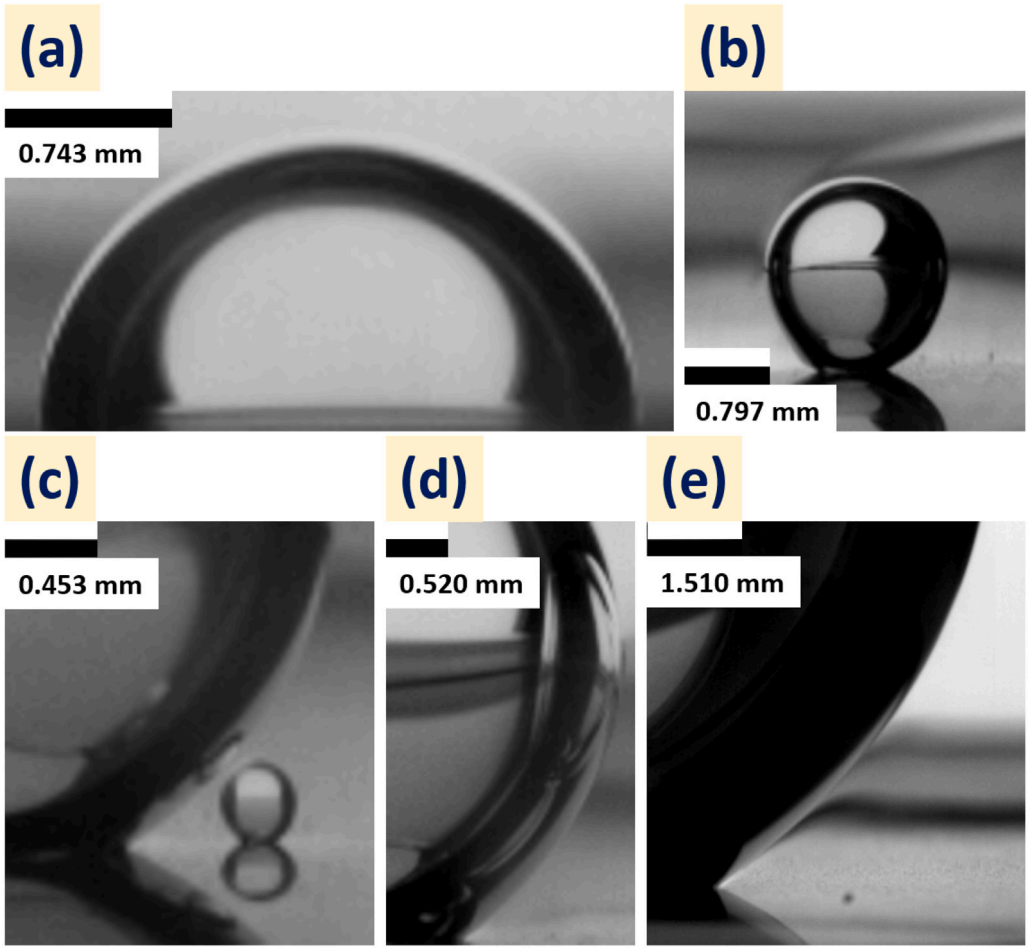

Fig. 1. Challenging cases of bubble boundary detection: (a) Weak gradient, (b) Vaporization structures, (c,d) Inter- and intra-bubble reflections, (e) Substrate reflection.

The boiling substrate is characterized by a heat transfer coefficient [11–15]. Heat is unevenly distributed in the scene, thus giving rise to optical distortions. The distortion is variable over time and is predominantly expressed above this substrate. Therefore, no assumptions are made as to the location of the substrate in the image.

No specific knowledge is assumed about the shape of the bubble contour. The proposed method traces the contour boundary in a pointwise fashion and, as such, can be used for asymmetric bubbles if needed. We make two assumptions. The first is specific to bubble formation and is that bubble contours are convex. The second is that bubble contours can be coarsely approximated with an ellipse. These assumptions simplify distinguishing edges that belong to one bubble from edges that belong to other bubbles.

The aforementioned phenomena are expressed in images in ways that confound conventional methods. Specifically, inter and intra-bubble reflections give rise to spurious edges, inhibiting the accuracy of edge-based approaches due to clutter. The lack of a strong gradient, due to highlights, misleads local, edge-based methods because the strongest edge is not always the correct one. Confounding image structures due to vaporization have similar shapes to the bubble contour, increasing the difficulty of the contour tracing task. In Fig. 1, indicative cases of these phenomena are shown. Image (a) shows that the contour's true boundary has a very weak gradient compared to the neighboring edges. Image (b) shows vaporization structures above the bubble. Images (c) and (d) show how complicated image structure near the boundary can be due to inter- and self-reflection. Image (e) shows the reflection of the substrate on the bottom part which causes the true bubble boundary to appear with less contrast than its neighboring edges.

1.2. This work

This work focuses on the accurate tracing of the bubble contour and proposes the grouping of edges as a way to increase the accuracy and robustness of edge-based approaches to bubble contour detection and measurement.

1.2.1. Legacy

The proposed method improves the method in [1] and [16, p. 9, Sec. 2.4]. We inherit the concept of working edges in polar images of bubbles and extend that work to acquire more refined contour tracings that lead to more accurate image measurements. Whereas in [1,16] we detected edges and directly fitted curves to them, in this work we propose an edge grouping approach to cope with the complex image structures and shortcomings of that work.

The proposed approach makes use of the so-called, "perceptual grouping" principles of Gestalt psychology. For an overview of these principles, we refer to [17]. The "continuity principle" promotes the grouping of continuous edges into perceptual wholes if they are aligned with each other. The grouped edges give rise to a "subjective contour" [18]. In this work, this contour is interpolated to generate contour edges not actually present in the image but inferred by the proposed method. This is in the same spirit where a subjective contour evokes the perception of edges without a luminance or color change across the locations of these "subjective edges" [18].

1.2.2. Novelty

A novel, edgel grouping approach is proposed tailored for the problem of tracing bubble contours of bubbles formed in microgravity.

This approach combines bottom-up and top-down cues in the grouping of edgels and accounts for the specific problem of bubbles that are growing and moving upon a subcooled substrate in microgravity.

The proposed method treats a problem that is overlooked by conventional methods, namely the occurrence of specular reflections upon the bubble surface. These reflections lead to a diminishment of image gradient, thereby misleading "edge-based" contour detectors because the true contour boundary in the image exhibits a smaller gradient magnitude than the spurious. To the best of our knowledge, this is the first method in the domain of vision-based, multiphase dynamic image analysis that employs perceptual grouping cues to recover the image boundary of bubbles.

Given the investigative nature of this study, there is difficulty in evaluating image-based methods due to the lack of explanatory physical laws that predict boiling bubble behavior under microgravity. Thereby, to the best of our knowledge, this is the first work that employs expert-based evaluation of contour tracing results for bubbles. This is achieved through the annotation of images by experts in a benchmark dataset that is publicly available for future research, improvements of this work, and comparative evaluation of pertinent methods.

1.3. Definitions and implementation notes

The monochromatic input image is denoted as I. The intensity of I at point $\mathbf{p} = [\mathbf{p}.x, \mathbf{p}.y]^T$ is denoted as $I(\mathbf{p})$. When $\mathbf{p}$ has non-integer coordinates, I is bilinearly interpolated.

Lens and perspective distortion are considered negligible. Rectifying for them will only improve the accuracy of the proposed method.

The detection of local maxima of 1D functions is performed with subpixel precision. A parabola is fitted to the preceding, current, and succeeding values of the maximum. The subpixel refinement of the maximum locus is analytically found, as the double root of the parabola equation. For 2D functions, this technique is applied independently, in the vertical and horizontal dimensions.

Edgels are individual pixels in whose vicinity the image intensity undergoes a sharp variation. Edges are sets of edgels that are neighboring and connected by an edgel linking algorithm.

Contact points are the image locations where the contour of the bubble meets the substrate. These points are two and distinguished as left and right. The localization estimates in I are denoted as $\mathbf{p}_l$ and $\mathbf{p}_r$, for the left and right contact points. Contact angles are the angles formed by the bubble and the substrate at these points.

A baseline is a line segment in I, where the interface of the bubble with the substrate is imaged. The baseline estimate is provided by $\mathbf{p}_l$ and $\mathbf{p}_r$. The image is horizontally aligned with the substrate and thus, the baseline is a horizontal line segment.

Figures are magnifiable, in the electronic version. The dimensions of the images are reported in Table 1 along with the area they image. In all images, the area imaged by 1 pixel is $.020245\,\mathrm{mm}^2$. In all figures and in Table 1 images are presented in left-to-right order. When multiple rows are present the order of rows is from top-to-bottom. Fig. 3 does not have a metric interpretation, because it refers solely to data structures stored as digital images.

Table 1
Image sizes (pixels) and corresponding imaged areas in the scene (mm).

Fig. 1
pixels: 110 × 56, 118 × 118, 67 × 77, 77 × 131, 224 × 251. mm: 2.23 × 1.13, 2.39 × 2.39, 1.36 × 1.56, 1.56 × 2.65, 4.53 × 5.08.
Fig. 2
pixels: 750 × 1100, 60 × 60, 80 × 80. mm: 15.18 × 22.27, 1.21 × 1.21, 1.62 × 1.62.
Fig. 3: all images
pixels: 249 × 45. mm: Not applicable
Fig. 4
pixels: 80 × 80. mm: 1.62 × 1.62.
Fig. 5: both rows
pixels: 80 × 80, 187 × 187, 151 × 151. mm: 1.62 × 1.62, 3.79 × 3.79, 3.06 × 3.06.
Fig. 6: all rows
pixels: 80 × 80, 187 × 187, 151 × 151. mm: 1.62 × 1.62, 3.79 × 3.79, 3.06 × 3.06.
Fig. 7: all images
pixels: 143 × 143. mm: 2.90 × 2.90.
Fig. 8
pixels: 183 × 183, 211 × 211, 234 × 234, 149 × 149, 159 × 159, 100 × 100, 76 × 76, 355 × 355. mm: 3.70 × 3.70, 4.27 × 4.27, 4.74 × 4.74, 3.02 × 3.02, 3.22 × 3.22, 2.02 × 2.02, 1.54 × 1.54, 7.19 × 7.19.
Fig. 9: same for all images
pixels: 700 × 700. mm: 14.17 × 14.17.

2. Related work

Image processing has been widely utilized to study the dynamics of a dispersed phase (bubbles, droplets) in multiphase systems, due to its non-intrusive nature [10,16,19,20]. However, existing image processing algorithms cannot be universally applied as they are quite sensitive to the imaging apparatus and are sensitive to illumination artifacts and background clutter. In the experiments encountered by this work, illumination artifacts include highlights and reflections that, along with image noise, give rise to spurious edges, which degrade the performance of contour tracing.

Therefore, in this section relevant work in the following topics is reviewed. Being a key contribution of this work, methods for the grouping of edgels are reviewed first, in Section 2.1. Next, in Section 2.2, model-based approaches to bubble detection are reviewed, followed by curve-fitting approaches, in Section 2.3. Finally, in Section 2.4, methods for the treatment of illumination artifacts are reviewed.

2.1. Edgel grouping

Edgel detection results obtained by conventional, local operators provide typically discontinuous results. Edgel grouping or linking methods, group edgels into continuous edges. Edges carry structure information which is useful in contour and object detection. A comprehensive review on the grouping of edgels and the discovery of contours in images can be found in [21]. Below, methods that are closely related to the proposed approach are reviewed.

Local grouping methods operate in small pixel neighborhoods and comprise the computational interpretation of the perceptual grouping principles [17] of proximity, continuity, and closure. Proximity-based principles postulate that the closer the edge points are, the more likely they are to be parts of the same edge. The simplest linking method is connected component labeling, where neighboring edgels are grouped in the same edge. Continuity-based principles suggest that for adjacent edgels to be parts of an edge they should be locally continuous. Although not producing edgel groups, the Canny [22] algorithm incorporates the proximity and continuity principles in its, third, hysteresis thresholding step, by suppressing weak edgels that are not connected to strong edges. Based on proximity, cocircularity, and smoothness, in [23] a path-based clustering approach is proposed. In [24,25], the continuity principle is employed to link edges in a hierarchical binary partition of the image.

Global grouping methods use the same principles, but employ a top-down approach to group edgels into edges. Active contours, or "snakes" [26] (see [27] for a review), are used to detect closed contours and are utilized as a means for image segmentation. Because they are agnostic to the segmentation targets, they are often used in medical imaging where image intensity represents radiance absorption rather than surface reflectance. Graph-based methods are employed to link edgels into close and smooth contours. The works in [28,29] encode proximity and continuity into a graph node linking cost which is optimized. In [30], boundary and regional cues are fused in a graph framework, to solve a closed-contour finding problem. Edgel grouping has been utilized by global methods to outline salient image regions using a convexity principle in [31], common fate in [32], and closure in [33].

In this work, the grouping of edgels combines bottom-up and top-down approaches. Specifically, the bottom-up, proximity and continuity cues are used to link edgels into edges in Section 3.5. Top-down cues, specifically convexity and common fate, are used in Section 3.6, to further group edges into edges that comprise candidate contour segments.

2.2. Model-based

Model-based methods [34–37] employ theoretical models of bubble shape in the form of analytical equations and use image measurements to estimate the parameters of these equations. Depending on the study, the bubble may be axis-symmetric which can be used to improve estimation accuracy [34]. In [38,39], circular bubbles are detected using the Hough transform. In [40,41], the initial detection based on the Hough transform is refined with the use of a template, a synthetic image that captures the appearance of the 'average' circular bubble. The method in [42] improves this approach, by utilizing multiple templates for different bubble appearances at multiple scales, and by detecting the rotated prototypes.

We cannot use model-based approaches, because this work targets the tracing of contour bubble shapes so that a model for these bubbles is achieved. If we would use a model at this stage, we would be introducing potentially unwanted biases in the shapes we provide. Moreover, bubble symmetry cannot be assumed in the boiling conditions evaluated.

2.3. Curve-fitting

A special case of model-based methods is those that fit curves locally, to estimate specific features of the bubble that are of interest to the study, specifically, the contact points and the apparent contact angles.

The points of the bubble contour in the vicinity of the contact points are used by curve-fitting methods to fit a polynomial rooted at the contact point and following as faithfully the shape of the contour, e.g. [43–47]. By doing so, the contact angle is analytically predicted by the tangent to the fitted polynomial, at its contact point. The model, in this case, is implicitly imposed by the type of polynomial that is used. A review of curve fitting methods for the approximation of the surface contour can be found in [48]. An open-source tool that incorporates multiple fitting methods is [10].

Relevant to this work is [49] in the sense that it also searches for the contour boundary across the direction perpendicular to the targeted contour. However, this method is generic, allows for concavities, and follows the strongest gradient to trace the contour which as earlier explained is a strategy we wish to avoid in the context of this work.

As in the case of Section 2.3, the goal of the proposed work is to trace the contour in the image, so that an appropriate modeling method utilizes the locations of the contour points. Of direct relevance to this work, is the sensitivity of contact angle measurements to small fluctuations of contour tracing, due to the use of high-order polynomials and the steep slope of the tangent function, which is considered in Section 4.

2.4. Treatment of illumination artifacts

Manual point-based annotation was employed in [50] to trace contours. Some works deal explicitly with the image structures due to bubble reflections. In [51], edges are linked into edge segments and, then, evaluated on their likelihood of belonging to a bubble based on its circularity. To further reduce spurious edges due to reflections, the inclusion of a segment inside another is evaluated and the inner segment is discarded. We use both of these ideas in this work, to discard spurious edges.

Active contours [26,52] were used in [53], however, they provided limited success because of inter-reflections and weak gradients near the true bubble contour. The reason is that the convergence of active contours is attracted from local gradient maxima. In the data, spurious local maxima with higher gradient magnitude than the correct ones are frequent. Moreover, image saturation in highlight regions causes the annihilation of gradient maxima at the image locations where the true bubble contour occurs.

Voting algorithms, based on the Hough transform [54] or RANSAC [55], have been used to group edgels that tend to form a circle or an ellipse against clutter [56,57]. They provided weaker results because they do not use the information provided by the grouping of edgels into edges. Due to the high clutter of our data, these methods often yield erroneous solutions, which "accidentally" accumulate voting edgels from multiple but incompatible edges. In this work, this problem is treated by requiring that either an entire edge participates in a configuration or not.

In [6], concentric and circular bubble arrangements are considered in an attempt to model the highlights appearing in scenes with multiple circular bubbles. The proposed work treats bubbles with greater shape variability than purely circular and is robust to illumination artifacts and reflections.

3. The proposed method

The proposed method consists of a pipeline of operations. A listing of its steps is provided as a guide to the next subsections.

Section 3.1: Input is image I. A background subtraction method on I provides a rough bubble contour, S. The points of S are used to initially approximate the, pursued, bubble contour with ellipse C.

Section 3.2: C is used to estimate the contact points locations $\mathbf{p}_l$ and $\mathbf{p}_r$.

Section 3.3: C is used to define the elliptical ring region $\mathcal{E}$ in I. This region, $I(\mathcal{E})$, is warped in orthogonal image V.

Section 3.4: The transformation of $I(\mathcal{E})$ into V simplifies the search for the bubble contour points in an (approximately) perpendicular direction to the direction of the pursued contour. The latter direction is approximated by the direction of C's contour at the corresponding location. Edgels are detected across the columns of V and linked into edges.

Section 3.5: These edges are used to locally approximate the bubble with circles. The ellipse is tessellated into elliptical sectors. In each one, the outermost group of edges that exhibits sufficient continuity is selected.

Section 3.6: The resultant contour is traced by interpolating the regional circles within their respective regions.

3.1. Coarse contour approximation

Input is I and S. Ellipse C is fit to the points of S using least-squares. C is our initial, coarse approximation of the bubble contour and is used to mark the elliptical ring $\mathcal{E}$ around it, within which we will search for the refined contour. This ring is computed by an enlargement and a reduction of C by scalar s, yielding an inner and an outer ellipse respectively.

In Fig. 2, the operation is illustrated. On the left, the original image is shown. The middle image shows S. The right image shows C (green) and the inner (red) and outer limits (blue) of $\mathcal{E}$.

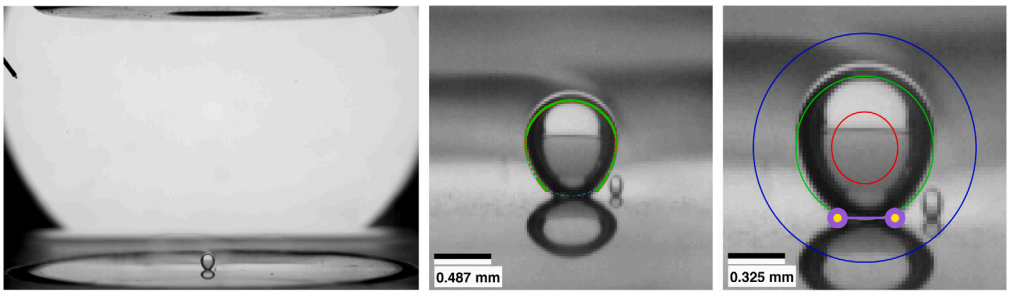

Fig. 2. Method initialization. Left: original image. Middle: coarse contour approximation. Right: elliptical ring $\mathcal{E}$ and contact points $\mathbf{p}_l$ and $\mathbf{p}_r$.

3.2. Baseline and contact point localization

The algorithm for detecting the baseline is as descripted in [1,16]. As there was no space in these publications and to better document the proposed method the details of its implementation are provided in Appendix A. In Fig. 2, the $\mathbf{p}_l$ and $\mathbf{p}_r$ and baseline found for that example are superimposed on the right image (mauve and yellow dots, mauve line segment).

We recall that the substrate is made from reflective material, giving rise to a bubble reflection and providing a visual cue to contact point detection. This visual cue is used to increase contact point localization accuracy. It ought to be noted that although this technique capitalizes on the reflection, the overall refinement method proposed in this work, is independent of the contact point detection method. As such, alternative methods can be used for this step, depending on imaging conditions.

3.3. Parameterization and polar image formation

The image region within the elliptical ring $\mathcal{E}$ is warped into polar image V, of $m \times n$ pixels. Its horizontal dimension maps orientation (Θ) and its vertical dimension (M) maps distance. The image formation equation is:

$$V(i,j) = I((a+\mu_j)\cos\theta_i, (b+\mu_j)\sin\theta_i). \tag{1}$$

The equation components are as follows. Let scaling range $M = [-u, u]$ ($u > 0$), where $u = s_r \cdot \max(a,b)$ and $s_r \in (0,1)$. Let also polar range $\Theta \subseteq [0, 2\pi)$. Ranges M and Θ are discretized in m and n equal steps, so that $\theta_i \in \Theta$, $\mu_j \in M$, $i \leq n$, $j \leq m$, and i, j are integers. Range Θ is constrained to start from the polar angle defined by $\mathbf{c}_l$ and end at the polar angle defined by $\mathbf{c}_l$. The resolution of V is set as per the Nyquist-Shannon sampling theorem [58,59]. Thus, the cardinality of M is $m = 2 \cdot (2u + 1)$ and the cardinality of Θ is twice the perimeter of $\mathcal{C}$.

We are not concerned with the part of the elliptical ring that is below the baseline. As such, polar image V is truncated to start at the polar coordinates of $\mathbf{p}_l$ and end at $\mathbf{p}_r$. Fig. 3 (top) shows V for the elliptical ring $\mathcal{E}$ of Fig. 2 (right).

3.4. Edgel and edge detection

To simplify the detection of edgels and edges we design a gradient function that responds strongly to intensity edges of orientation locally compatible with that of the bubble and responds weakly to incompatible orientations. We consider as our gradient the second order, partial derivative of V. The magnitude of this gradient is $L = |\partial^2 V / \partial y^2|$ and is a $m \times n$ image. Due to the polar parameterization of V, the compatible orientations are those predicted by our coarse approximation of the bubble, ellipse $\mathcal{C}$.

The second-order derivative is used because the bubble contour is formed by slope edges and its appearance in the image ends at the end of the slope, which is given by the local maximum of the Laplacian [60]. Thereby, local maxima are detected across each column of V, with sub-pixel accuracy, as 1D local maxima. Their locations mark the resultant slope edgels.

Some of the edgels of interest exhibit very low contrast. We maximize the sensitivity of edge detection to respond to elemental variations of intensity and accept, as edges, all local minima that have a gradient higher than a very small threshold τ_g. Typically, this gives rise to a plethora of spurious edgels. However, using the proposed gradient incompatible edgels are inhibited.

Finally, edgels are linked into edges with 8-neighbor connectivity and by suppressing "junctions", or otherwise edges with more than two neighbors. Thus, all edges are linear and delimited by their extremal points.

In Fig. 3, the gradient magnitude (2nd row), the detected edgels (3rd row), and the detected edges (bottom) for V (top) are shown. In Fig. 4, conventional edge detectors [22] (left), [61] (2nd from left) are compared with the proposed one (3rd from left), by superimposing edgel detection results on I. The same intensity threshold was used in the three detections. The linked edges detected by the proposed method are shown in Fig. 4 (right), using the same color coding as in Fig. 3 (bottom). To fairly compare subpixel precision, [22,61] were applied to a 4× bicubic interpolated upsampling of the original image. We observe that the proposed edge detection yields less and more relevant edgels with respect to the pursued contour boundary.

3.5. Edge grouping

To approximate the local bubble shape we group edges that we trust to belong to the contour of the bubble. We trust better the groups of edges that exhibit sufficient continuity (see Section 1.2) and iteratively select the outermost of them.

Because the curvature and the local shape of the bubble contour vary across arclength, $\mathcal{C}$ is partitioned into sectors. Each sector contains a number of edges, let n, and is treated iteratively. In the experiments, we found 3 sectors sufficient, though this is a tunable algorithmic parameter. Sectors were overlapping by an angular span of τ_o.

In each sector, edges are grouped according to their suitability in forming a group of well-aligned curve segments that may potentially approximate the bubble contour and, iteratively, find the outermost one. The iterations refine local estimate $\mathbf{c}_f$ which is a curve initialized with $\mathcal{C}$. This curve may be an ellipse or a circle and is dependent on the type of experiment (see Section 4). In the first case, the dimension of the curve is $\delta = 3$ and in the latter $\delta = 5$.

In each iteration, we consider the n edges in that sector and evaluate their $2^n - 1$ combinations. We discard combinations that (1) include overlapping edges, (2) exhibit low density, (3) do not exhibit sufficient continuity, or (4) are incompatible with the size of the bubble. These are achieved as follows.

1. Due to the polar parameterization, the overlap of two segments is evaluated by comparing only their first and last horizontal polar coordinates; see variable i in Eq. (1). As segments do not contain junctions (see Section 3.4), the task is reduced to the overlap detection of two 1D intervals. This interval can be found

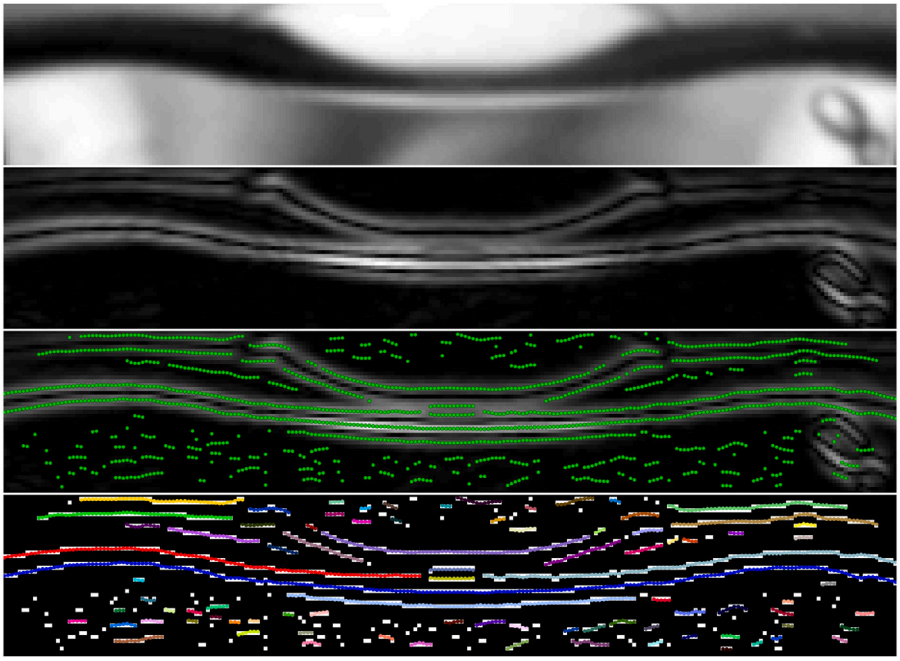

Fig. 3. Top to bottom: polar image V, gradient magnitude L, edgel, and edge detection.

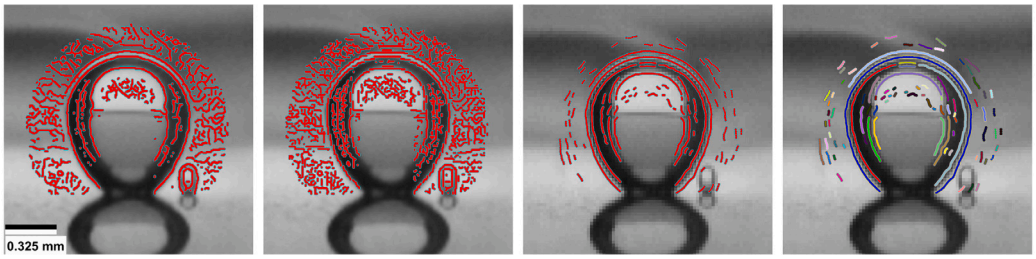

Fig. 4. Left to right: Canny, Sobel, proposed edgel detection, and linked edgels detected by the proposed method. Scale legend for the leftmost image is the same for all images of this figure.

as $[\max(\alpha_1, \beta_1), \min(\alpha_2, \beta_2)]$ for intervals $[\alpha_1, \alpha_2]$, $[\beta_1, \beta_2]$ and has a span of zero in case of no overlap.

2. Density is evaluated as the count of edgels of the combination, normalized over the angular span of the sector. More specifically, we consider the edgels of edges whose mean distance from the current version of $\mathbf{c}_f$ is lower than threshold τ_d. This promotes combinations that are well aligned with the current estimate of the bubble contour, as provided by $\mathbf{c}_f$.
3. Continuity is evaluated by fitting a new curve, let $\mathbf{c}'_f$, to all edgels of the combination and measuring their distances from the curve. The mean value of these distances indicates the goodness of fit. A high value means that the curve did not fit well the edgels of the candidate combination and, thus, the combination is rejected if this distance is above threshold τ_c. If the combination is valid, then $\mathbf{c}'_f$ is associated with the combination.
4. Size compatibility is evaluated only for combinations that exhibit continuity. The area of $\mathbf{c}'_f$ associated with the combination is compared to the area of C. The combination is invalidated if the two areas differ by a factor of τ_κ.

The suitability of valid combinations is quantified with the following objective function $o = \rho \cdot \gamma \cdot \lambda$, where ρ is the radius or length of the major axis of $\mathbf{c}_f$, if $\delta = 3$ or $\delta = 5$ respectively, γ is the angular span of the combination, and λ is the number of edgels in the combination. The combination with the best score is kept and the curve $\mathbf{c}'_f$ is associated with it. Curve $\mathbf{c}_f$ is updated with $\mathbf{c}'_f$ and edges inside $\mathbf{c}'_f$, in that sector, are discarded. This operation is repeated with any edges remaining and terminates when no more edges remain. The last $\mathbf{c}_f$ is the result for the sector.

To increase the generality of the approach, a scale factor was introduced to adapt the values of spatial parameters according to bubble size. This scale factor, σ, was obtained as the 5% of the largest of the two axes of C. Threshold τ_c is defined as a function of σ, in Section 4.

A computational simplification comes from the polar parameterization of V. Edges that are inside the bubble contour are identified once contact points are localized. The vertical coordinates of $\mathbf{p}_l$ and $\mathbf{p}_r$ in V define a line, above which the edges detected correspond to edges inside the bubble and are directly removed from candidates.

In Fig. 5, this iterative operation is illustrated, for the same sector, in three example cases. The figures in the top row show the detected edges, after the removal of "inner edges". The second row illustrates the operation over the two iterations required for these three examples. The green curve and points correspond to the first iteration, blue to the second, and red for the third. The result for the three cases is the red curve and the yellow edges are rejected as they are outside it. In the left and middle columns $\delta = 3$ and in the right $\delta = 5$.

3.6. Contour tracing

In the previous version, to trace the contour, we computed the outermost edgel for each orientation in Θ. Capitalizing on bubble convexity, this work computes the convex hull of the outermost points.

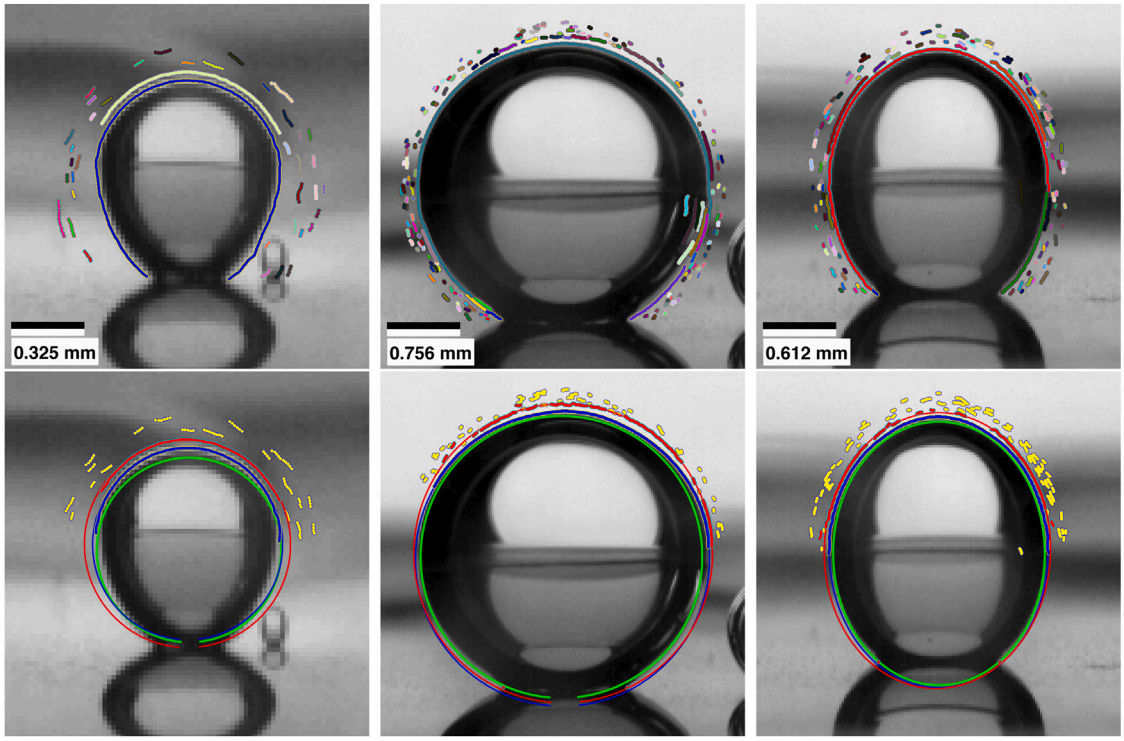

Fig. 5. Edge grouping. Top: filtered edges. Bottom: iterative edge grouping. The initial curve is green. The curves due to the 1st and 2nd iterations are blue and red respectively. Yellow edges are discarded. Scale legends for images in the bottom row are the same as for the corresponding images in the upper row.

Thereafter, we use the same sectors as in Section 3.5 and fit curve $\mathbf{c}_t$ at each sector.

We use the $\mathbf{c}_t$ associated with each sector, to interpolate the bubble contour in that sector. Interpolation generates contour points at a step distance of half a pixel. Points $\mathbf{p}_l$ and $\mathbf{p}_r$ are concatenated at the beginning and at the end of this point list, respectively.

The purpose of this interpolation is to compensate for locations of the bubble contour that have zero or close to zero gradient magnitude and do not give rise to edgels. That is to implicitly infer the contour that is consistent with the outermost edges detected, even if parts of the contour are missing, such as in the case of subjective contours. The improvement due to this operation is shown in Fig. 6, where the middle column shows the contour tracing result of the previous method and the right column the output of the proposed method.

4. Experiments

The experiments took place in a boiling cell filled with test fluid, in which a laser beam hits a designated location on a substrate to produce isolated bubbles at that location. Variable conditions lead to images of wide diversity. Analytical information and details about the apparatus and physical interpretation of these experiments can be found in [1]. To the best of our knowledge, this is the first work that provides ground truth annotations for the particular dataset.

In the presented experiments the performance of this work is compared against software that was authored for the study of boiling in microgravity. We chose to compare this method with the best-performing method from [1] (see Section 4.5), as this is the most relevant work to the proposed one.

4.1. Data

The input images are monochromatic and their size is 1100×750 pixels. The benchmark data sets can be found in [1]. The data include 15 image sequences and are publicly available.[1] In Table 2 the names of the sequences are shown. For brevity, datasets are denoted as D1 to D15, as in the aforementioned table. Each image sequence consists of 5000 images and includes $\approx$ 500 frames imaging an empty boiling chamber just before the first bubble is formed. The data fall into three experimental conditions, each containing bubbles of different morphology. The names of the conditions are shear flow (D1–D5), pool boiling (D6–D9), and electric field (D10–D15).

Table 2 shows the experimental conditions applied during each benchmark boiling experiment. The test cell is filled with the liquid bulk at the desired pressure (P) and subcooling temperature (T_{sub}) conditions. The heater surface provides some heat flux (HF) to the liquid. Some time after heater activation (t_{wait}), a laser pulsation triggers nucleation of the first boiling bubble on the heater surface. Q is the liquid flow rate in shear flow experiments and V is the voltage of the electric field in the same called experiments.

Shear flow experiments exhibit multiple, simultaneous, relatively small, and moving bubbles towards the left of the chamber. When a new bubble is formed, the older one slides towards the left. A characteristic of this condition is that, due to bubble motion, asymmetries are observed between contact angles. In addition, due to the small size of bubbles, the distortion due to thermal gradient is expressed upon a significant portion of the bubble area. We are particularly interested in this condition because it addresses asymmetric bubbles and the measurement of the differences between left and right contact angles. The reason is that the differences between them are minute and, thus, accurate and precision measurements are significant to reliably distinguish systematic differences between the two.

Electric field experiments produce large, immobile, and elongated bubbles of elliptical shape. Pool boiling sequences record a single immobile bubble that monotonically grows, eventually occupying most of the chamber. These two conditions are treated using symmetric contour fits.

[1] Download link https://doi.org/10.48328/tudatalib-1059.

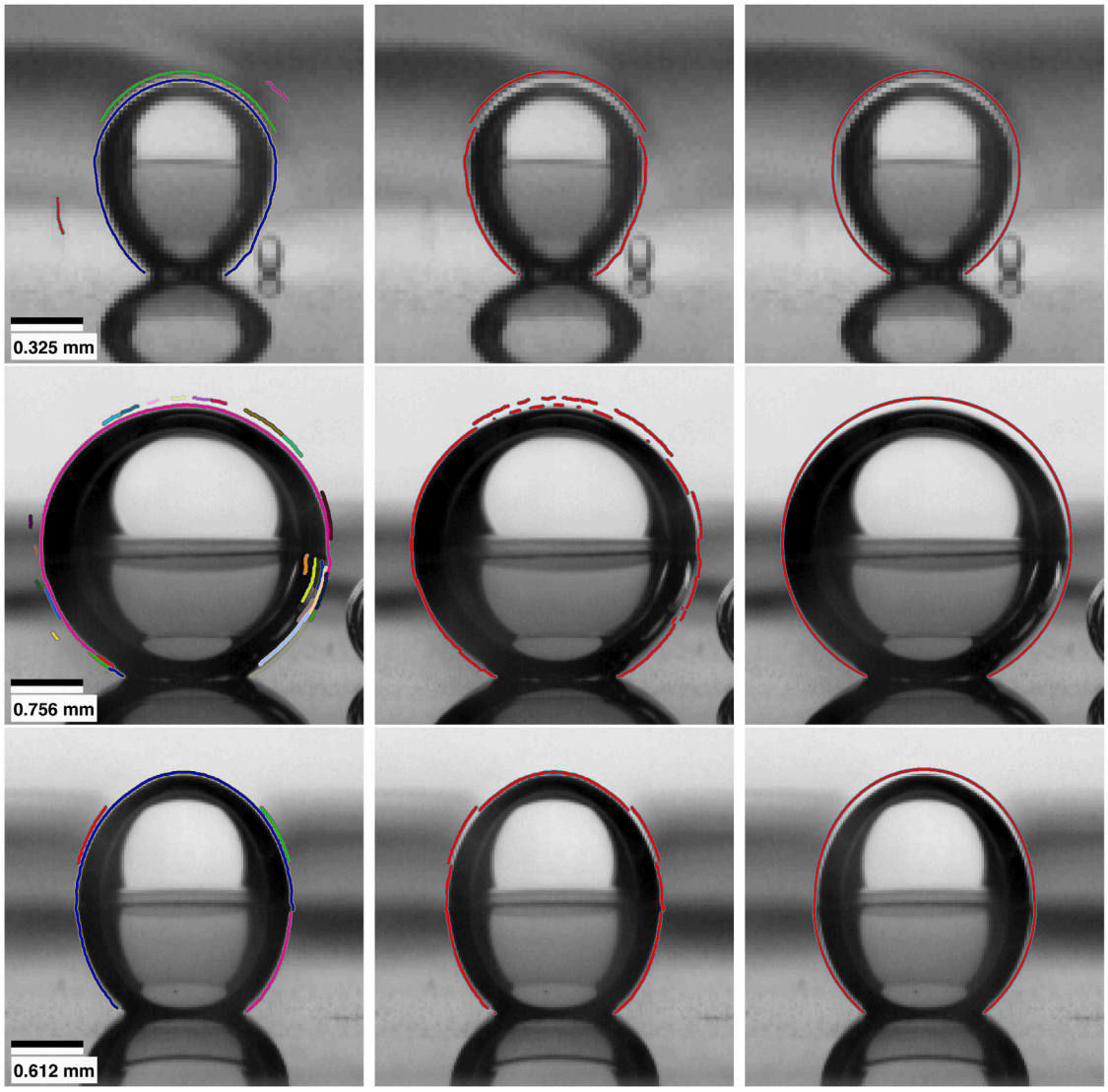

Fig. 6. Contour tracing. Left: detected edges, Middle: trusted points. Right: traced contour. Scale legends shows in the images of the left column are the same for all images of the corresponding row.

Table 2
Experimental conditions for the benchmark datasets. Units: P, $(mbar)$; T_{sub} (°C); HF (W/cm^2); Q (ml/min); t_{wait} (ms); V (kV).

#	id	P	T_{sub}	HF	Q	t_{wait}	V
1	EAS-dDd-C00aDc-01	1000	10	1.5	100	5	0
2	EAS-dDd-C00cDc-01	1000	10	1.5	500	5	0
3	EAS-dBc-000aBc-02	1000	3	1.0	100	2	0
4	EAS-dBc-000cBc-01	1000	3	1.0	500	2	0
5	EAS-dBa-C00cBc-01	1000	3	0.5	500	2	0
6	EAP-dBc-0000Dc-01	1000	3	1.0	0	5	0
7	EAP-dCa-0000Ec-03	1000	5	0.5	0	10	0
8	EAP-cBc-0000Bc-02	750	3	1.0	0	2	0
9	EAP-aAc-0000Dc-03	500	1	1.0	0	5	0
10	EAE-bCc-0cA0Ec-01	600	5	1.0	0	10	15
11	EAE-bCc-0bA0Ec-01	600	5	1.0	0	10	10
12	EAE-bCc-0aA0Ec-01	600	5	1.0	0	10	5
13	EAEb-Ac0-cA0Ac-01	600	1	1.0	0	1	15
14	EAEc-Bd0-cA0Ac-01	750	3	1.5	0	1	15
15	EAEd-Ca0-aA0Ac-01	1000	5	0.5	0	1	5

4.2. Ground truth

To measure the error of the proposed method ground truth on the bubble contours was obtained through visual annotation of bubble contours in the acquired images. Error measurements were obtained by comparing the contour annotations with the contours produced by the proposed method, on the same images.

The annotation assignment was the localization of contact points and several contour points, so an adequate contour description was obtained, according to the judgment of the expert. The annotators used custom-made software to pinpoint samples upon contour locations in the images carefully, using magnification, undo, and editing facilities. The experts annotated the contact points and multiple points on the contour of the bubble until they were satisfied with the result. The annotators were two multiphase dynamics experts (SE, OO) and one image processing expert (ICS).

The annotations were collected for the first bubble of each data set. For each bubble, 20 frames were sampled in chronological order and in equidistant temporal steps and annotated. All experts annotated data sets D1–D5. ICS annotated the rest after learning annotation insights from SE and OO. The annotations can be found in [62].

4.3. Evaluation rationale

To benchmark the accuracy and precision of the proposed method we compare the contact point locations, the areas, and the shapes of the computed, K_1, and annotated, K_2, contours. To benchmark robustness, we measure how errors in contour tracing affect the computation of contact angles.

Contact points are local features and their localization accuracy is measured in pixel distanceas $e = |u_e - u_g|$, where u_e and u_e are the horizontal coordinates of the estimated and ground truth points, respectively. The errors for the left and right contact points are denoted as e_l and e_r, respectively.

The contour area is measured in square pixels. Area comparison serves as a measure of method accuracy. Because bubbles grow during boiling, areas are compared by their percentage difference $\nu = (K_1 - K_2)/K_1$.

Shape comparison targets the precision of the method and measures spatial discrepancies between K_1 and K_2. A symmetric measure of area difference is used, normalized by the area of their union. Binary masks M_1 and M_2 are computed, to be the same size as I and true at the pixels on and in K_1 and K_2, respectively. The areas of union and intersection of these contours are scalars $\mu_{1\cup2}$ and $\mu_{1\cap2}$. Contour dissimilarity is a percentage measure quantified as $\omega = (\mu_{1\cup2} - \mu_{1\cap2})/\mu_{1\cup2}$. The smaller this measure is, the better the tracing of the contour is regarded.

Contact angle measurement is sensitive to "jitter" in contour tracing. Due to the tangential computation of angle, small variations in contour tracing can lead to large variability in contact angle estimates. We use the robustness measures, to compare the robustness of (a) and (b), given that the bubble contour grows continuously over time. Our evaluation of robustness uses the variability of angle value during a sliding time interval. A moving median of $c = 7$ points approximates the "noise-free" angle value along time. The absolute angular difference of the estimate with the corresponding median value quantifies local variability. The computation of this measure is as follows:

$$\epsilon = \frac{\sum_{i=1}^{c} |\zeta_i - M_c|}{c}, \tag{2}$$

where M_c is the median value in the c-point neighborhood and ζ_i is the ith value of that neighborhood. As such, the smaller this measure is, the better the robustness of the tracing is regarded.

Several approaches to contact angle measurement based on curve fitting exist (see Section 2). We follow [1,16], which are tailored to the specific study. The reason is the additional image distortion by the propagation of heat in the liquid bulk of the test cell during each experiment [63,64]. As such, the bottom part of the contour is not considered in the computation of the contact angle. Therefore, in shear flow experiments, we fit a circle to the contour points that belong to the top left (L) quadrant of the contour and analytically predict the tangent at the contact point, as in [1,16]. We do equivalently for the right top quadrant (R) and contact angle. For reference, we also fit a circle to all contour points (F) and another circle to the upper half points (T). Pool boiling and electric field experiments deal with symmetric bubbles; thus, we fit an ellipse to all contour points (F) and another to the upper half points (T). For the robustness evaluation, we used all the frames of the first bubble of each dataset.

For all measures, when more than one ground truth annotations are available, the aforementioned measures are computed independently and averaged into a single value. When referring to the "ground truth area" of a bubble, we refer to the average area of contours of the available annotations.

The proposed method is agnostic to the temporal sampling rate of images and, thus, time is measured in frames. For reference only, we note that (a) the image acquisition rate was 500 frames per second and (b) at the focus distance of the camera, a pixel distance in the image corresponds to $\approx .01$ mm in the imaged scene.

4.4. Execution

In all experiments, the domain of I was $[0, 1]$, $s_r = 50\%$, $\tau_o = 10°$, $\tau_g = 10^{-3}$, $\tau_d = 25\%$, $\tau_c = \sigma/10$, and $\tau_\kappa = 10$. Due to the morphology of bubbles in different conditions, the dimension of curves $\mathbf{c}_f$ was $\delta = 3$ sufficient for all experiments except the electric field ones, in which $\delta = 5$.

Background subtraction is implemented using the 500 images of the scene devoid of bubbles, averaged into a 'training image'. The pixel-wise, absolute differences between the current and the training image were used to roughly detect the silhouettes of bubbles in the current image, using connected component labeling ("blob" detection).

We applied the proposed method to all benchmark data sets, for all bubbles, and all frames. The traced contours are shown for all bubbles and all frames in [65]. The videos contain illustrations and numerical readings of contact angle estimates (see below).

A MATLAB implementation of the proposed approach takes about 72 hours to process all 15 benchmark data sets on a single core of an i7 CPU. The processing can be accelerated if multiple cores are available, by parallelizing the processing of data sets.

4.5. Results

First, we evaluate the accuracy of the traced contours using the ground truth annotations, to compare contact point localization and contour area estimation. Second, we evaluate robustness using contact angle estimates. In the experiments, we compare the performance of the most relevant and best-performing method in this problem which is [1], denoted as (a), with the proposed one denoted as (b).

We illustrate the improvement due to the proposed approach by observing the change that it brings to conventional contour tracing and in the estimates of contact angles. Fig. 7, shows the same contour tracing operation performed on the trusted points provided by the previous and the proposed method. The example comes from a Pool Boiling experiment and, specifically, from the D8 sequence. The images on the left side of the figure belong to frame 934 of that sequence. The left column shows the trusted points for (a, top) and (b, bottom), and the middle column the traced contour for (a, top) and (b). When edges are missing, contour tracing results in an inaccurate contour, which is determined by nearby spurious edges. By interpolating upon the found, "subjective" contour we obtain more accurate results. We also study the entire sequence of the occurrence of this bubble and the contact angles estimated in each frame. The example is from a pool boiling experiment and so, an ellipse is fitted to estimate these angles (see Section 4.3) and a single angle value is reported. An ellipse is fitted to all points (F) and another one to the upper half points (T). The top-right graph compares the "full" fits for the two methods and the bottom-right graph "top" fits for the two methods. The proposed method exhibits better continuity which indicates a more robust result.

In Appendix B, the contact angle estimates of the proposed method for the first bubble of all benchmark sequences are provided in the same type of plots. The discrepancies are more pronounced at the beginning of the sequence, where the bubble is small and errors of a few pixels have a greater effect on the estimated contact angle. This appendix serves also as an ablation study in which certain subsets of the trusted points are removed in order to understand their contribution to overall performance.

A first ablation experiment regarded the type of edge detector employed. Specifically, we substituted the proposed edge detector with the conventional edge detectors, Canny and Sobel, when detected edges in V. The results were inferior leading to error almost an order of magnitude greater in all metrics. This failure is attributed to the generality of these edge detectors which led to contour concavities. This does not mean that these edge detectors are inferior, but that the proposed one accounts for prior knowledge in the given problem (bubble convexity).

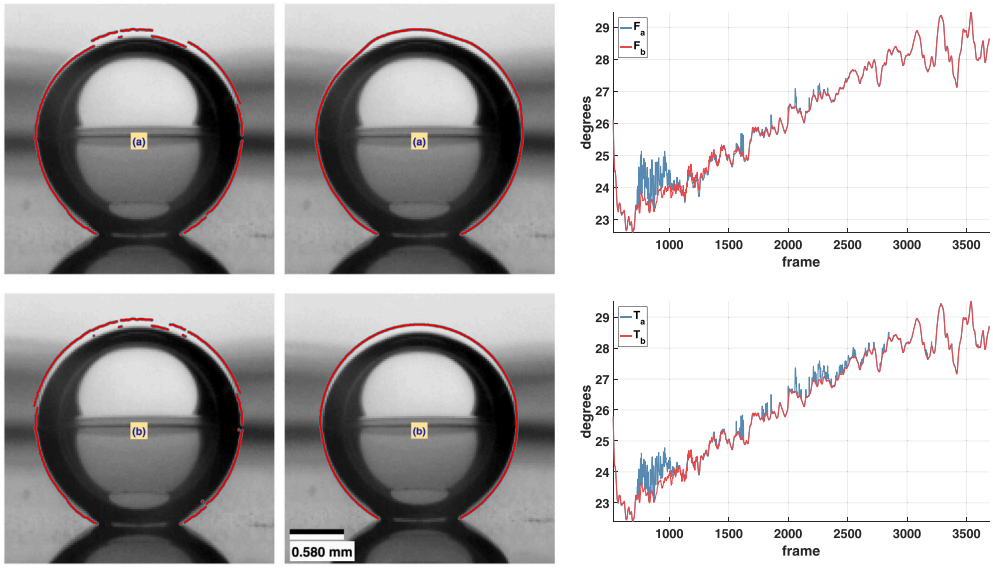

Fig. 7. Comparison of contour tracing and contact angle estimates. Top: method (a). Bottom: method (b). Left column: trusted point detection. Middle column: Contour tracing. Right column: the top plot shows contact angle estimates for fitting condition (F) and the bottom plot for fitting condition (T). Scale legend in the bottom right image is the same for all images of this figure.

A second ablation experiment regarded the edge detection sensitivity parameter τ_g. We found this to be the most critical parameter for the proposed method. The reason is that when raised edge sensitivity decreases and, thus, weak edges occurring at the top of the bubble which is shiny are undetected. The utilized value (10^{-3}) is set so that it is well below the smallest intensity variation in our images, which is $\tau_{min} = 1/255 \approx 4 \cdot 10^{-3}$. When this parameter is increased above τ_{min} we have observed a gradual deterioration of the method's accuracy. This deterioration leads to the same effect and fluctuations observed in Fig. 9 in Section 4.6, below.

Tables 3, 4, and 5 report the error measures for D1–D15, for the annotated frames. In the tables, row 1 notes the dataset number, in boldface, and, on its right, the number of frames corresponding to the first bubble. Row 2 provides a reference for the image area μ of the bubble, noting the ground truth areas for the first and last annotated contours, in thousands of square pixels ($10^3 \cdot p^2$). Row 3 reads the e_l, e_r localization errors, in pixels (p). Rows 4 and 5 compare the contour tracing of (a) and (b), using the ground truth annotations. Specifically, row 4 notes the area error measures (ν_a, ν_b) and row 5 the shape similarity measures (ω_a, ω_b).

The last rows of Tables 3, 4, and 5 compare the robustness of (a) and (b). For the shear flow experiments (Table 3), row 6 corresponds to the fit for all points (F) and row 7 to the fit for the upper half points (T). Row 8 compares the left fits (L) and row 9 compares the right fits (R). Quantities F, T, L, and R are calculated using Eq. (2). In the pool boiling and electric field conditions (Tables 4 and 5), the bubbles are symmetric, and, thus, rows 8 and 9 are omitted. Robustness evaluation does not make use of the ground truth annotations and so, it is based on all the dataset frames.

4.6. Observations

We observe a slight but identifiable improvement in accuracy on macroscopic spatial features, such as the area and similarity. We attribute this to the refinement nature of the proposed method that affects details of contour shape, while area and similarity regard hundreds or thousands of pixels.

The improvement brought by the proposed method is better observed when studying features that depend on accurate and precise contour tracing, such as the value of the contact angle and, specifically,

Table 3
Error and robustness quantification for the shear flow data sets for methods (a) and (b). Method (b) is shown in bold. The measurements are presented in five pairs of columns. The top row notes the dataset number (bold) and the number of frames that the first bubble occurs. Row 2: bubble size growth. Row 3: left and right contact point localization error. Rows 4 and 5: area and shape similarity errors. Rows 6 to 9: robustness measurements. Units: μ ($10^3 \cdot p^2$); $\mathbf{p}_{l,r}$ (p); $\nu_{a,b}$; $\omega_{a,b}$, $F_{a,b}$, $T_{a,b}$, $L_{a,b}$, and $R_{a,b}$ (%).

	1	2049	**2**	939	**3**	1499	**4**	459	**5**	777
μ	0.8	8.1	0.7	2.9	1.0	28.2	1.0	77.7	0.8	2.9
$e_{l,r}$	0.9	1.1	0.7	1.5	1.1	2.1	1.0	1.9	0.8	1.6
$\nu_{a,b}$	0.9	**0.8**	2.9	**2.1**	1.5	**1.7**	1.1	**1.1**	0.6	**0.5**
$\omega_{a,b}$	2.5	**2.3**	3.4	**3.4**	3.6	**2.4**	2.7	**1.9**	2.5	**2.4**
$F_{a,b}$	1.5	**1.2**	3.1	**2.1**	4.1	**1.8**	4.5	**3.9**	2.6	**2.1**
$T_{a,b}$	1.4	**1.2**	2.8	**1.8**	4.3	**1.8**	3.9	**3.8**	2.8	**2.0**
$L_{a,b}$	7.6	**2.9**	14.3	**5.8**	40.8	**5.6**	14.0	**5.0**	24.0	**3.5**
$R_{a,b}$	9.0	**3.9**	9.9	**5.4**	58.8	**8.0**	20.5	**5.3**	15.3	**2.9**

Table 4
Error and robustness quantification for the pool boiling data sets. Rows 1 to 5: as in Table 3. Rows 6 and 7: robustness measurements. Units as in Table 3.

	6	2497	**7**	4181	**8**	3199	**9**	2991
μ	0.5	27.4	0.3	8.1	0.4	42.1	1.5	82.5
$e_{l,r}$	0.4	0.6	0.3	0.4	0.5	0.7	0.6	0.8
$\nu_{a,b}$	1.4	**1.4**	1.3	**1.2**	1.1	**1.1**	1.1	**1.1**
$\omega_{a,b}$	1.9	**1.8**	3.4	**3.1**	2.2	**2.1**	1.6	**1.6**
$F_{a,b}$	1.2	**1.3**	3.1	**0.8**	2.8	**1.5**	0.3	**0.4**
$T_{a,b}$	1.1	**1.5**	2.9	**1.1**	2.4	**1.8**	0.2	**0.5**

Table 5
Error and robustness quantification for the electric field data sets. Rows and units as in Table 4.

	10	586	**11**	795	**12**	1534	**13**	582	**14**	940	**15**	4497
μ	0.7	10.0	0.8	13.3	0.8	21.6	0.5	62.3	0.3	7.4	0.1	1.8
$e_{l,r}$	0.3	0.6	0.3	0.5	0.4	0.6	0.3	0.3	0.3	0.3	0.2	0.2
$\nu_{a,b}$	1.0	**1.3**	1.0	**1.2**	0.7	**1.3**	0.8	**1.4**	0.9	**1.7**	1.8	**2.6**
$\omega_{a,b}$	2.4	**2.2**	2.2	**2.0**	3.3	**1.5**	3.1	**2.5**	3.4	**2.9**	4.6	**4.0**
$F_{a,b}$	5.1	**5.0**	4.1	**3.8**	21.6	**2.5**	10.3	**6.9**	6.2	**3.9**	2.5	**2.0**
$T_{a,b}$	7.3	**5.9**	5.4	**4.2**	48.7	**3.2**	10.6	**8.8**	6.6	**5.0**	2.9	**2.7**

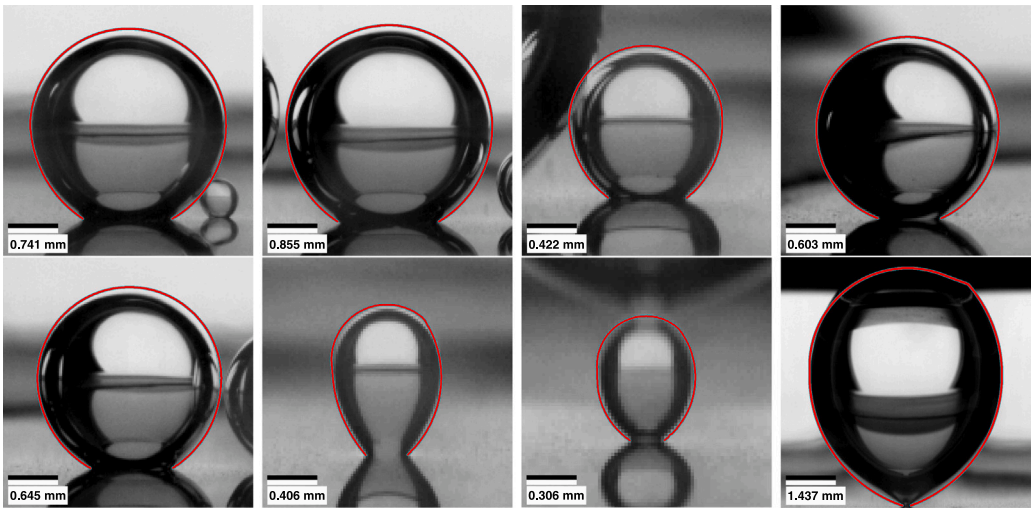

Dataset	3	3	3	4	4	10	10	12
Bubble	3	4	6	3	14	1	4	1
Frame	2487	3193	3816	1416	3149	550	2382	2038

Fig. 8. A gallery of characteristic contour tracings obtained from the proposed method. The table below marks the dataset, the bubble number in the dataset (in order of appearance), and the frame number of the dataset which the image is taken from.

the robustness of the proposed method to noise. Quantitatively, this can be observed in Tables 3, 4, and 5. Qualitatively, this can be observed by comparing the contact angle curves plots in Fig. B.11 with their corresponding ones in [16] . We stress that in the plots of Fig. B.11 the vertical axis spans only a few degrees.

Comparatively, the estimates obtained by the (F) and (T) exhibit greater robustness because they are based on more points. However, these two fits are symmetric and do differentiate between the estimated left and right contact angles, which are different particularly in the shear flow experiments. The right and left contact angle fits show this difference more pronounced when the bubble is in motion. Similarly, a high degree of robustness is found in the pool boiling and electric field experiments, as a single curve is fit over the same arclength proportion.

The robustness to the rapid effects encountered in boiling and the occurrence of multiple bubbles is the main advantage brought by the proposed work. In Fig. 8, we provide the contour tracings computed by the proposed work for a gallery of challenging cases. As can be observed in the supplementary videos in [65], the contact angle estimates are robust to the generation of new bubbles and vibrations, which affect bubble shape, and the estimates follow this shape with fidelity.

A measurement limitation is observed in D3 during approximately the last third of the sequence. In the corresponding images, the gradient at the top of the bubble is very weak or zero and, as a result, there is a fluctuation in the tracing of the boundary which can be observed in the measurements of contact angle values, in Fig. B.11 (top, right). A visual example of this limitation is provided in Fig. 9. Shown are five consecutive frames, from frame 1597 to 1601 of sequence D3. The fluctuation can be observed at the top of the bubble, where the shiny part of the bubble has the same intensity value as the background. Its effect is a fluctuation of $\approx 2°$ in the contact angle estimates. The effect can be closely inspected in the supplementary videos [65]. For such cases, other measurement approaches that use only lower parts of the bubble found in [1,16], can be more appropriate. Independently of the contact angle calculation approach, the improvement due to the proposed method is retained since the contour tracing, upon which this calculation is based, is more accurate.

5. Conclusion and future work

A method for detecting bubble contours in images of boiling bubbles in microgravity was proposed. This method improves the accuracy and robustness of previous ones designed for the same purpose. The proposed method refines an initial contour approximation obtained from conventional background subtraction and was designed to cope with a wide variety of visual phenomena that hinder contour detection using traditional approaches. This is achieved, by the iterative grouping of edges that are continuous and compatible with the bubble shape. A data set annotated by ground truth was contributed [62], which can be used to measure the accuracy and precision of bubble detection and measurement methods. The proposed method is quantitatively evaluated using the ground truth evaluation. The method results are visualized in videos that are provided as supplementary material [65].

This method is provided as a single image analysis method. The obtained results can be filtered afterward either through an elementary approach (i.e., smoothing) or by optimal estimators, i.e. Kalman filtering [66], by treating curves $\mathbf{c}_f$ as state variable vectors.

The implementation of the proposed method is experimental and implemented in an interpreted programming language (MATLAB script), rather than in a compiled one. As such it can be accelerated, just by rewriting it in a compiled language, e.g., C. Next to it, parallelisable image processing operations, i.e., image warping and gradient computation, implemented on a general programming GPU would further improve computational performance.

An investigation that we warrant is the adaption of the regions and thresholds pertaining to edge detection, after the first run of the proposed method. That is, run a second pass, to constrain edge detection per contour point in a narrow, local region around the first localization of this point. This means constraining the search for edges in a small region of each column of V, individually for each column. Moreover, the edge detection threshold can be adapted individually for each column, either to reduce candidate edges when many or to provide at least some edges when the gradient is weak.

The main disadvantage of the proposed approach is its exponential computational cost in Section 3.5. Usually, this feature does not take a devastating toll on the execution time of the method. The reason is that for small and medium-sized bubbles there are only a few edges per investigated region. However, when a bubble grows to a large size, e.g. in the pool boiling experiments, then execution time for a single bubble can take up to half an hour on a regular personal computer. A numerical optimization that leads to the same results

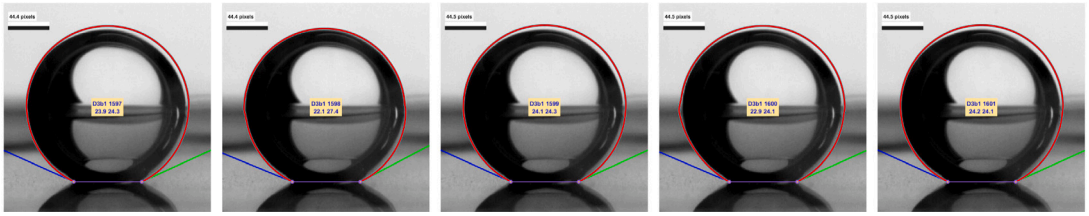

Fig. 9. Fluctuations in the top part of the traced contour due to weak or zero gradient. Images illustrate the estimated contact points, the traced bubble contour, and the estimated contact angles. Each image shows the dataset, bubble number, and frame number, in the center of the bubble. Below this reading, the estimates of the contact angles are printed. Scale legend in pixels.

without exhaustively evaluating all possible hypotheses is warranted for future work.

Finally, we aim to study the efficacy of global optimization methods for image segmentation [49,67–70] as well as active contours, by adapting their objective function for the particular case of bubble contour tracing in microgravity.

CRediT authorship contribution statement

Xenophon Zabulis: Methodology, Software, Validation, Writing – original draft, Writing – review & editing, Conceptualization. **Polykarpos Karamaounas:** Software, Visualization, Validation. **Ourania Oikonomidou:** Investigation, Data curation, Formal analysis, Conceptualization, Supervision. **Sotiris Evgenidis:** Investigation, Data curation, Formal analysis, Conceptualization, Supervision. **Margaritis Kostoglou:** Data curation, Formal analysis. **Martin Schinnerl:** Data curation, Resources, Supervision, Project administration, Funding acquisition. **Axel Sielaff:** Investigation, Data curation, Conceptualization, Formal analysis, Supervision, Project administration, Funding acquisition. **Peter Stephan:** Conceptualization, Resources, Supervision, Project administration, Funding acquisition. **Thodoris Karapantsios:** Conceptualization, Resources, Supervision, Project administration, Funding acquisition.

Declaration of competing interest

The authors declare that they have no known competing financial interests or personal relationships that could have appeared to influence the work reported in this paper.

Data availability

Data will be made available on request

Acknowledgments

The present work has been carried out in the framework of the European Space Agency Research projects AO-2004-111: BOILING, AO-1999-110: EVAPORATION, AO-2004-096: CONDENSATION. We thank all the Multiscale Boiling Science Team Members of the different institutions for their contribution in making possible the implementation of the experiment on-board the International Space Station: Technical University of Darmstadt, Institute for Technical Thermodynamics; Aix-Marseille University, IUSTI; University of Pisa; Institute of Thermal-Fluid Dynamics, ENEA; Institut de Mécanique des Fluides de Toulouse; Aristotle University of Thessaloniki; Transfers Interfaces and Processes, Université Libre de Bruxelles; University of Ljubljana; Kutatteladze Institute of Thermo-physics, Novosibirsk.

The authors would also like to gratefully thank ESA, and in particular Daniele Mangini, Olivier Minster, Anne Pacros, Balazs Toth, and Marco Braibanti for their interest and support of the activities linked to Multiscale Boiling, and for the fruitful discussions. They would also like to thank AIRBUS (with particular gratitude to the project manager, Olaf Schoele-Schulz), as well as B.USOC for the kind cooperation (and especially Carla Jacobs and Denis Van Hoof) during all the pre-flight, in-flight and post-flight operations.

Co-authors from the Technical University of Darmstadt would like to thank the German Aerospace Center (DLR) for the financial support in the framework of the Vapor II and Vapor III projects, grant no. 50WM2257 and 50W1959, respectively.

The authors thank the anonymous reviewers for their constructive criticism, helpful, and meaningful comments and corrections. The authors also thank Antonis A. Argyros for the internal review.

Appendix A. Baseline localization

Image I is aligned with the substrate surface and, thus, the baseline is imaged as a horizontal line segment at image row β. Due to the reflection of the bubble, the baseline is also the axis of an (approximate) local image symmetry. Initially, we coarsely approximate row β in which the baseline occurs using this symmetry. Next, we refine this approximation by detecting the contact points based on the image gradient. Its left and right endpoints of the baseline are denoted as $\mathbf{c}_l$ and $\mathbf{c}_r$, respectively.

The coarse approximation of β optimizes local image symmetry in the intensity domain. This approximation is found using the support of w_0 image rows. The value of β that optimizes image symmetry is found iteratively. Initially, $i = 0$ and β_0 is the y-value of the lowest point of S.

Sub-images I_u and I_d of image I are formed as functions of β_i and w_i.

$$\begin{aligned} I_u(\beta_i, w_i) &= I(R_u(\beta_i, w_i), W); \\ I_d(\beta_i, w_i) &= I(R_d(\beta_i, w_i), W), \end{aligned} \tag{A.1}$$

where R_u and R_d are two ranges of rows and W is a range of columns. Range $W = [\mathbf{c}.x - r, \mathbf{c}.x + r]$ remains constant through the optimization. Ranges R_u and R_d are modulated as

$$\begin{aligned} R_u(\beta_i, w_i) &= [\beta_i - w_i, \beta_i - 1]; \\ R_d(\beta_i, w_i) &= [\beta_i + 1, \beta_i + w_i]. \end{aligned} \tag{A.2}$$

Thus, at each iteration, a thinner support of rows is evaluated.

Accounting for the inversion of vertical coordinate order due to the reflection, we quantify dissimilarity, or asymmetry, between I_u and I_d as:

$$\mathcal{O}(I_u, I_d) = \sum_{j=1}^{w_i} \sum_{k=1}^{2r+1} |I_u(j,k) - I_d(w_i - j, k)|. \tag{A.3}$$

The value β_i that optimizes $\mathcal{O}()$ is:

$$\beta_i = \arg\max_{\beta_i} [(I_u(\beta_i, w_i), I_d(\beta_i, w_i))] \tag{A.4}$$

and comprises the ith estimate of the baseline row. This estimate is iteratively refined, using β_{i+1} as the new initial estimate and halving support as $w_i = w_0/2^i$. The search ends when $w_i < 1$ and the result is $\beta_c = \beta_i$. In each iteration, we compute the intersections of the horizontal line at row β_i with C. In the vicinity of these intersections, we detect the points where gradient magnitude is maximized. We call these points

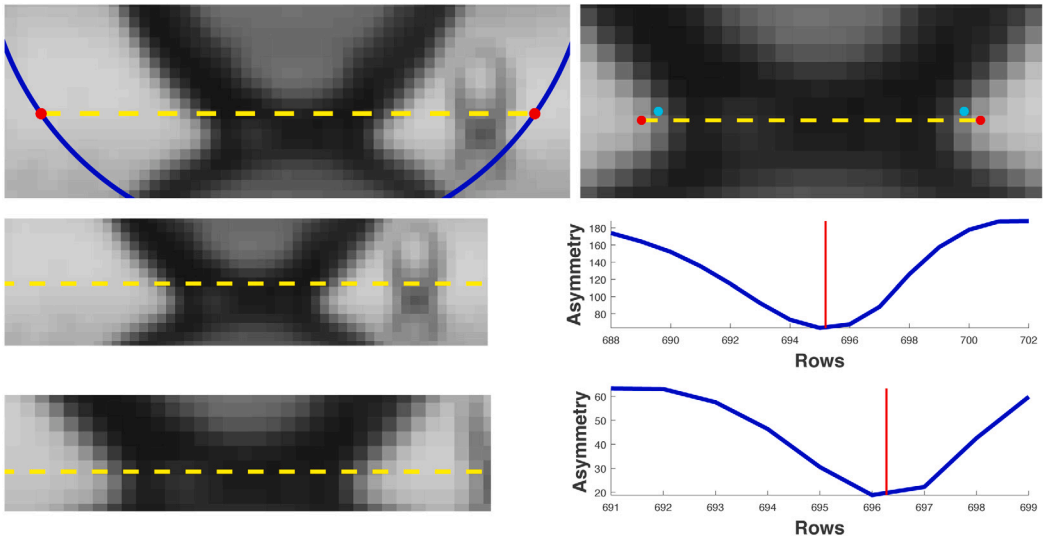

Fig. A.10. Baseline localization. Top left: elliptical ring $\mathcal{E}$, coarse baseline approximation b_0, and their intersections. Image size: 40 × 58. Top right: initial baseline and contact point localization and refined result. Image size: 14 × 54. Middle and bottom rows: iterative refinement of the contact point and baseline localization (left) and plot of the function $\mathcal{O}()$ (right).

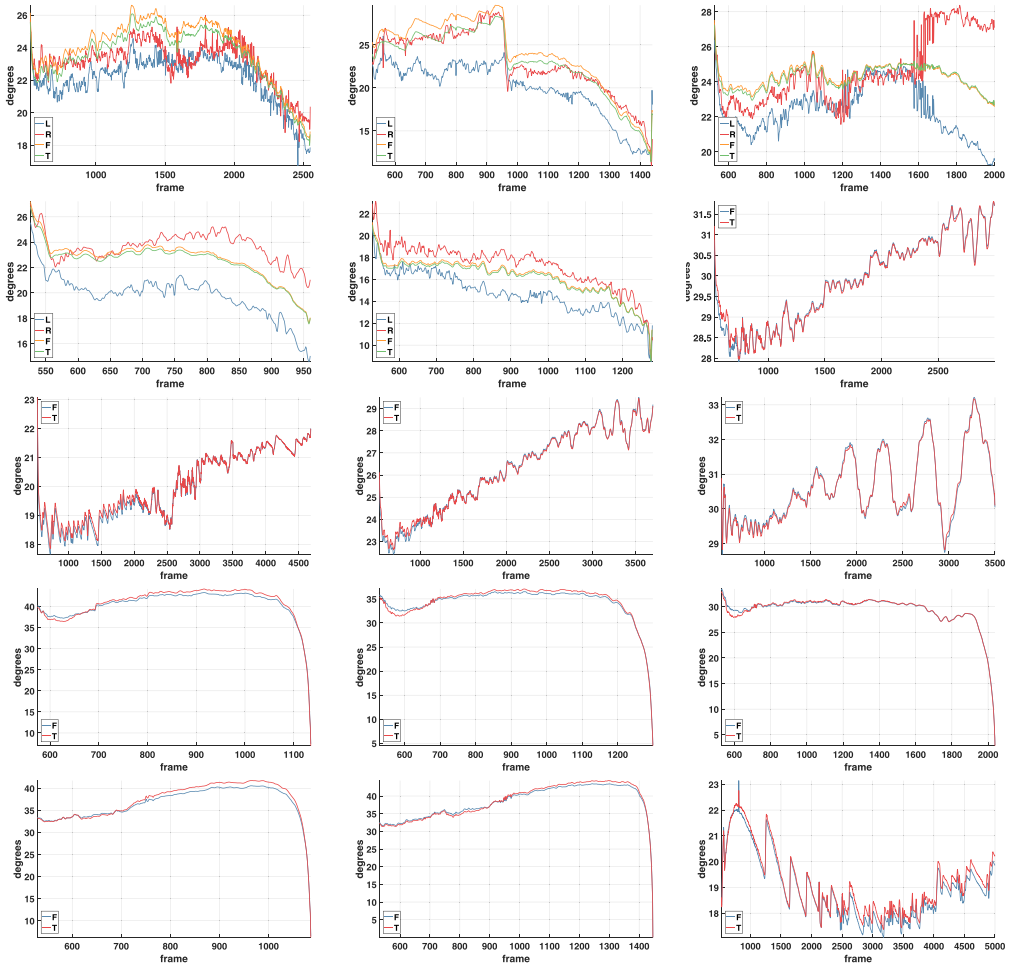

Fig. B.11. Contact angle measurement per dataset and per frame for the first bubble of D1–D15. Plot order is row-wise and left-to-right.

intermediate contact points and update the current values of $\mathbf{c}_l$ and $\mathbf{c}_r$ with these locations.

Using this coarse approximation, the intersections of the outer limit of $\mathcal{E}$ with line β are found. We employ corner detection [71] at the vicinity of these intersections to refine the contact point locations. The vertical coordinates of $\mathbf{c}_l$ and $\mathbf{c}_r$ are set to their average, as well as the final value of β. These comprise the final estimation of the baseline segment.

The value of w_0 and the spatial extent of the corner detector are set according to image scale and resolution. In all experiments of this work, $w_0 = 7$ leads to 2 iterations of the similarity optimization. Also, the corner detector used a 7×7 pixel kernel.

In Fig. A.10, this process is illustrated. The top left image plots b_0 as a (yellow) dashed line and its intersections with the outer limit of $\mathcal{E}$, which is plotted with a continuous (blue) line. In the two bottom rows, the two iterations of the symmetry optimization are illustrated; the penultimate row corresponds to the first iteration and the last to the second iteration. On the left shown of these two rows shown are I_u and I_d concatenated as a single image. The dashed lines plot β_1 and β_2. The plotted points mark the intermediate refinements of the contact points. On the right of these two rows shown is the asymmetry score plot with a (blue) continuous like as a function of the evaluated image row. The vertical (red) line marks the retrieved minimum in subpixel precision, which corresponds to the values of β_1 and β_2. The top right image plots the final results of contact point localization connected with a dashed line at the final value of β. The individual (cyan) dots mark the last locations of the intermediate contact points, prior to corner detection.

Appendix B. Contact angle estimates

In Fig. B.11, the plots of contact angle estimates are shown, for each first bubble, of the 15 benchmark data sets. For shear flow experiments, four curves are plotted as the experiments consider asymmetric bubbles. The rest of the experiments consider symmetric bubbles and, thus, plot two curves. The naming of curves in the legends is as in Section 4.

Appendix C. Supplementary data

Supplementary material related to this article can be found online at https://doi.org/10.1016/j.measurement.2023.113644.

References

[1] A. Sielaff, D. Mangini, O. Kabov, M. Raza, A. Garivalis, M. Zupančič, S. Dehaeck, S. Evgenidis, C. Jacobs, D. Van Hoof, O. Oikonomidou, X. Zabulis, P. Karamaounas, A. Bender, F. Ronshin, M. Schinnerl, J. Sebilleau, C. Colin, P. Di Marco, T. Karapantsios, I. Golobič, A. Rednikov, P. Colinet, P. Stephan, L. Tadrist, The multiscale boiling investigation on-board the International Space Station: An overview, Appl. Therm. Eng. 205 (2022) 117932, http://dx.doi.org/10.1016/j.applthermaleng.2021.117932.

[2] S. Hong, J. Wang, Z. Gao, C. Dang, Review on state-of-the-art research in pool and flow boiling under microgravity, Exp. Therm Fluid Sci. 144 (110848) (2023) 1–19, http://dx.doi.org/10.1016/j.expthermflusci.2023.110848.

[3] A. Luke, D. Cheng, High speed video recording of bubble formation with pool boiling, Int. J. Therm. Sci. 45 (3) (2006) 310–320, http://dx.doi.org/10.1016/j.ijthermalsci.2005.06.011.

[4] G. Thorncroft, J. Klausnera, R. Mei, An experimental investigation of bubble growth and detachment in vertical upflow and downflow boiling, Int. J. Heat Mass Transfer 41 (23) (1998) 3857–3871.

[5] M. Sattari, L. Mahdavian, Thermodynamic properties of the bubble growth process in a pool boiling of water-ethanol mixture two-component system, Open Chem. 17 (1) (2019) 88–95, http://dx.doi.org/10.1515/chem-2019-0010.

[6] N. Strokina, J. Matas, T. Eerola, L. Lensu, H. Kalviainen, Detection of bubbles as concentric circular arrangements, Mach. Vis. Appl. 27 (2016) 387–396, http://dx.doi.org/10.1007/s00138-016-0749-7.

[7] M. Mirzaei, A new method for measuring the contact angles from digital images of liquid drops, Micron 102 (2017) 65–72, http://dx.doi.org/10.1016/j.micron.2017.09.001.

[8] S. Siedel, S. Cioulachtjian, J. Bonjour, Experimental analysis of bubble growth, departure and interactions during pool boiling on artificial nucleation sites, Exp. Therm Fluid Sci. 32 (8) (2008) 1504–1511, http://dx.doi.org/10.1016/j.expthermflusci.2008.04.004.

[9] X. Ren, G. Xiang, C. Zhang, Y. Duan, Application of MOG background subtraction algorithm in automatic measurement of contact angle, J. Phys. Conf. Ser. 1650 (2020) 032087, http://dx.doi.org/10.1088/1742-6596/1650/3/032087.

[10] R. Akbari, C. Antonini, Contact angle measurements: From existing methods to an open-source tool, Adv. Colloid Interface Sci. 294 (2021) 102470, http://dx.doi.org/10.1016/j.cis.2021.102470.

[11] N. Schweizer, P. Stephan, Experimental study of bubble behavior and local heat flux in pool boiling under variable gravitational conditions, Multiph. Sci. Technol. 21 (4) (2009) 329–350, http://dx.doi.org/10.1615/MultScienTechn.v21.i4.40.

[12] A. Karchevsky, I. Marchuk, O. Kabov, Calculation of the heat flux near the liquid-gas-solid contact line, Appl. Math. Model. 40 (2) (2016) 1029–1037, http://dx.doi.org/10.1016/j.apm.2015.06.018.

[13] M. Gibbons, P. Di Marco, A. Robinson, Local heat transfer to an evaporating superhydrophobic droplet, Int. J. Heat Mass Transfer 121 (2018) 641–652, http://dx.doi.org/10.1016/j.ijheatmasstransfer.2018.01.007.

[14] J. Jo, J. Kim, S. Kim, Experimental investigations of heat transfer mechanisms of a pulsating heat pipe, Energy Convers. Manage. 181 (2019) 331–341, http://dx.doi.org/10.1016/j.enconman.2018.12.027.

[15] K. Schweikert, A. Sielaff, P. Stephan, Heat flux during dip-coating of a superheated substrate, Interfacial Phenom. Heat Transf. 7 (3) (2019) 269–281, http://dx.doi.org/10.1615/InterfacPhenomHeatTransfer.2019032623.

[16] O. Oikonomidou, S. Evgenidis, C. Argyropoulos, X. Zabulis, P. Karamaoynas, M. Raza, J. Sebilleau, F. Ronshin, M. Chinaud, A. Garivalis, M. Kostoglou, A. Sielaff, M. Schinnerl, P. Stephan, C. Colin, L. Tadrist, O. Kabov, P. Di Marco, T. Karapantsios, Bubble growth analysis during subcooled boiling experiments onboard the international space station: Benchmark image analysis, Adv. Colloid Interface Sci. 308 (2022) 102751, http://dx.doi.org/10.1016/j.cis.2022.102751.

[17] J. Elder, R. Goldberg, Ecological statistics of Gestalt laws for the perceptual organization of contours, J. Vision 2 (4) (2002) 5, http://dx.doi.org/10.1167/2.4.5.

[18] G. Kanizsa, Subjective contours, Sci. Am. 234 (4) (1976) 48–53, http://dx.doi.org/10.1038/scientificamerican0476-48.

[19] A. Garivalis, P. Di Marco, Life of a single bubble growing within an electric field in microgravity: some preliminary results of the reference mUltiscale Boiling Investigation, J. Phys. Conf. Ser. 2116 (1) (2021) 012008, http://dx.doi.org/10.1088/1742-6596/2116/1/012008.

[20] E. Somm, F. Jornayvaz, Fibroblast Growth Factor 15/19: From Basic Functions to Therapeutic Perspectives, Endocr. Rev. 39 (6) (2018) 960–989, http://dx.doi.org/10.1210/er.2018-00134.

[21] Y. Daipeng, P. Bo, A. Zaid, M. Asad, Z. Donghai, An overview of edge and object contour detection, Neurocomputing 488 (2022) 470–493, http://dx.doi.org/10.1016/j.neucom.2022.02.079.

[22] J. Canny, A computational approach to edge detection, IEEE Trans. Pattern Anal. Mach. Intell. 8 (6) (1986) 679–698, http://dx.doi.org/10.1109/TPAMI.1986.4767851.

[23] B. Fischer, J. Buhmann, Path-based clustering for grouping of smooth curves and texture segmentation, IEEE Trans. Pattern Anal. Mach. Intell. 25 (4) (2003) 513–518, http://dx.doi.org/10.1109/TPAMI.2003.1190577.

[24] S. Alpert, M. Galun, B. Nadler, R. Basri, Detecting faint curved edges in noisy images, in: K. Daniilidis, P. Maragos, N. Paragios (Eds.), European Conference in Computer Vision, Springer Berlin Heidelberg, Berlin, Heidelberg, 2010, pp. 750–763, http://dx.doi.org/10.1007/978-3-642-15561-1_54.

[25] N. Ofir, M. Galun, B. Nadler, R. Basri, Fast detection of curved edges at low SNR, in: IEEE Conference on Computer Vision and Pattern Recognition, 2016, pp. 213–221, http://dx.doi.org/10.1109/CVPR.2016.30.

[26] M. Kass, A. Witkin, D. Terzopoulos, Snakes: Active contour models, Int. J. Comput. Vis. 1 (4) (1988) 321–331, http://dx.doi.org/10.1007/BF00133570.

[27] P. Giuseppe, P. Nicolai, Edge and line oriented contour detection: State of the art, Image Vis. Comput. 29 (2) (2011) 79–103, http://dx.doi.org/10.1016/j.imavis.2010.08.009.

[28] S. Wang, T. Kubota, J. Siskind, Salient boundary detection using ratio contour, in: International Conference on Neural Information Processing Systems, MIT Press, Cambridge, MA, USA, 2003, pp. 1571–1578.

[29] J. Stahl, S. Wang, Edge grouping combining boundary and region information, IEEE Trans. Image Process. 16 (10) (2007) 2590–2606, http://dx.doi.org/10.1109/TIP.2007.904463.

[30] Y. Ming, H. Li, X. He, Winding number constrained contour detection, IEEE Trans. Image Process. 24 (1) (2014) 68–79, http://dx.doi.org/10.1109/TIP.2014.2372636.

[31] S. Wang, J. Stahl, A. Bailey, M. Dropps, Global detection of salient convex boundaries, Int. J. Comput. Vis. 71 (2007) 337–359, http://dx.doi.org/10.1007/s11263-006-8427-2.

[32] C. Chen, J. Corso, Joint occlusion boundary detection and figure/ground assignment by extracting common-fate fragments in a back-projection scheme, Pattern Recognit. 64 (2017) 15–28, http://dx.doi.org/10.1016/j.patcog.2016.10.013.

[33] S. Mahamud, L. Williams, K. Thornber, K. Xu, Segmentation of multiple salient closed contours from real images, IEEE Trans. Pattern Anal. Mach. Intell. 25 (4) (2003) 433–444, http://dx.doi.org/10.1109/TPAMI.2003.1190570.

[34] S. Saad, A. Neumann, Axisymmetric drop shape analysis (ADSA): An outline, Adv. Colloid Interface Sci. 238 (2016) 62–87, http://dx.doi.org/10.1016/j.cis.2016.11.001.

[35] H. Chen, J. Muros-Cobos, A. Amirfazli, Contact angle measurement with a smartphone, Rev. Sci. Instrum. 89 (2018) 035117, http://dx.doi.org/10.1063/1.5022370.

[36] A. Vazquez, R. Sanchez, E. Salinas-Rodríguez, A. Soria, R. Manasseh, A look at three measurement techniques for bubble size determination, Exp. Therm Fluid Sci. 30 (1) (2005) 49–57, http://dx.doi.org/10.1016/j.expthermflusci.2005.03.018.

[37] G. McHale, H. Erbil, M. Newton, S. Natterer, Analysis of shape distortions in sessile drops, Langmuir 17 (22) (2001) 6995–6998, http://dx.doi.org/10.1021/la010476b.

[38] O. Ronneberger, W. Qing, H. Burkhardt, Fast and robust segmentation of spherical particles in volumetric data sets from brightfield microscopy, in: IEEE International Symposium on Biomedical Imaging: From Nano to Macro, 2008, pp. 372–375, http://dx.doi.org/10.1109/ISBI.2008.4541010.

[39] B. Taboada, L. Vega-Alvarado, M. Córdova-Aguilar, E. Galindo, G. Corkidi, Semi-automatic image analysis methodology for the segmentation of bubbles and drops in complex dispersions occurring in bioreactors, Exp. Fluids 41 (2006) 383–392, http://dx.doi.org/10.1007/s00348-006-0159-0.

[40] A. Rojas Dominguez, G. Corkidi, Automated recognition of oil drops in images of multiphase dispersions via gradient direction pattern, in: International Congress on Image and Signal Processing, Vol. 3, 2011, pp. 1209–1213, http://dx.doi.org/10.1109/CISP.2011.6100481.

[41] S. Maass, J. Rojahn, R. Hansch, M. Kraume, Automated drop detection using image analysis for online particle size monitoring in multiphase systems, Comput. Chem. Eng. 45 (2012) 27–37, http://dx.doi.org/10.1016/j.compchemeng.2012.05.014.

[42] X. Zabulis, M. Papara, A. Chatziargyriou, T. Karapantsios, Detection of densely dispersed spherical bubbles in digital images based on a template matching technique: Application to wet foams, Colloids Surf. A 309 (1) (2007) 96–106, http://dx.doi.org/10.1016/j.colsurfa.2007.01.007.

[43] F. Chini, A. Amirfazli, A method for measuring contact angle of asymmetric and symmetric drops, Colloids Surf. A 388 (1) (2011) 29–37, http://dx.doi.org/10.1016/j.colsurfa.2011.08.001.

[44] E. Atefi, J. Mann, H. Tavana, A robust polynomial fitting approach for contact angle measurements, Langmuir 29 (19) (2013) 5677–5688, http://dx.doi.org/10.1021/la4002972, PMID: 23570502.

[45] A. Bateni, S. Susnar, A. Amirfazli, A. Neumann, A high-accuracy polynomial fitting approach to determine contact angles, Colloids Surf. A 219 (1) (2003) 215–231, http://dx.doi.org/10.1016/S0927-7757(03)00053-0.

[46] L. Li, W. Kang, D. Ye, A contact angle measurement method for the droplets in EWOD-based chips, in: IEEE International Conference on Nano/Micro Engineered and Molecular Systems, 2007, pp. 1071–1075, http://dx.doi.org/10.1109/NEMS.2007.352203.

[47] I. Ríos-López, P. Karamaoynas, X. Zabulis, M. Kostoglou, T. Karapantsios, Image analysis of axisymmetric droplets in wetting experiments: A new tool for the study of 3D droplet geometry and droplet shape reconstruction, Colloids Surf. A 553 (2018) 660–671, http://dx.doi.org/10.1016/j.colsurfa.2018.05.098.

[48] K. Law, H. Zhao, Surface Wetting: Characterization, Contact Angle, and Fundamentals, Springer, Cham, 2016, pp. 7–34, http://dx.doi.org/10.1007/978-3-319-25214-8_2 (Chapter Contact Angle Measurements and Surface Characterization Techniques).

[49] Z. Yin, R.T. Collins, Shape constrained figure-ground segmentation and tracking, in: IEEE Conference on Computer Vision and Pattern Recognition, 2009, pp. 731–738, http://dx.doi.org/10.1109/CVPR.2009.5206674.

[50] D.-C. Cheng, H. Burkhardt, Bubble tracking in image sequences, Int. J. Therm. Sci. 42 (7) (2003) 647–655, http://dx.doi.org/10.1016/S1290-0729(03)00030-9.

[51] C. Paz, M. Conde, J. Porteiro, M. Concheiro, On the application of image processing methods for bubble recognition to the study of subcooled flow boiling of water in rectangular channels, Sensors 17 (6) (2017) http://dx.doi.org/10.3390/s17061448.

[52] X. Chenyang, J. Prince, Snakes, shapes, and gradient vector flow, IEEE Trans. Image Process. 7 (3) (1998) 359–369, http://dx.doi.org/10.1109/83.661186.

[53] R. al Darwich, L. Babout, K. Strzecha, An edge detection method based on local gradient estimation: Application to high-temperature metallic droplet images, Appl. Sci. 12 (14) (2022) http://dx.doi.org/10.3390/app12146976.

[54] R. Duda, P. Hart, Use of the hough transformation to detect lines and curves in pictures, Commun. ACM 15 (1) (1972) 11–15, http://dx.doi.org/10.1145/361237.361242.

[55] M. Fischler, R. Bolles, Random sample consensus: A paradigm for model fitting with applications to image analysis and automated cartography, Commun. ACM 24 (6) (1981) 381–395, http://dx.doi.org/10.1145/358669.358692.

[56] O. Martorell, A. Buades, J. Lisani, Multiscale detection of circles, ellipses and line segments, robust to noise and blur, IEEE Access 9 (2021) 25554–25578, http://dx.doi.org/10.1109/ACCESS.2021.3056795.

[57] F. Duan, L. Wang, P. Guo, RANSAC based ellipse detection with application to catadioptric camera calibration, in: Neural Information Processing. Models and Applications, Springer Berlin Heidelberg, Berlin, Heidelberg, 2010, pp. 525–532, http://dx.doi.org/10.1007/978-3-642-17534-3_65.

[58] C. Shannon, Communication in the presence of noise, in: Proceedings of the Institute of Radio Engineers, Vol. 37, IRE, 1949, pp. 10–21, http://dx.doi.org/10.1109/proc.1984.12998.

[59] H. Nyquist, Certain topics in telegraph transmission theory, Trans. Am. Inst. Electr. Eng. 47 (1928) 617–644, http://dx.doi.org/10.1109/T-AIEE.1928.5055024.

[60] H. Chidiac, D. Ziou, Classification of image edges, in: Vision Interface, 1999, pp. 17–24.

[61] N. Kanopoulos, N. Vasanthavada, R. Baker, Design of an image edge detection filter using the sobel operator, IEEE J. Solid-State Circ. 23 (2) (1988) 358–367, http://dx.doi.org/10.1109/4.996.

[62] X. Zabulis, P. Karamaounas, O. Oikonomidou, S. Evgenidis, M. Kostoglou, A. Sielaff, P. Stephan, T. Karapantsios, Ground Truth Annotations for Boiling Bubble Detection and Measurement in Microgravity, Zenodo, 2023, http://dx.doi.org/10.5281/zenodo.7553797.

[63] S. Narayan, A. Srivastava, S. Singh, Rainbow schlieren-based investigation of heat transfer mechanisms during isolated nucleate pool boiling phenomenon: Effect of superheat levels, Int. J. Heat Mass Transfer 120 (2018) 127–143, http://dx.doi.org/10.1016/j.ijheatmasstransfer.2017.12.005.

[64] S. Narayan, A. Srivastava, S. Singh, Rainbow schlieren-based direct visualization of thermal gradients around single vapor bubble during nucleate boiling phenomena of water, Int. J. Multiph. Flow. 110 (2019) 82–95, http://dx.doi.org/10.1016/j.ijmultiphaseflow.2018.08.012.

[65] X. Zabulis, P. Karamaounas, O. Oikonomidou, S. Evgenidis, M. Kostoglou, M. Schinnerl, A. Sielaff, P. Stephan, T. Karapantsios, Bubble Measurement Results for Boiling Bubbles in Microgravity, Zenodo, 2023, http://dx.doi.org/10.5281/zenodo.7609605.

[66] R. Kalman, A new approach to linear filtering and prediction problems, J. Basic Eng. 82 (1) (1960) 35–45, http://dx.doi.org/10.1115/1.3662552.

[67] Y. Boykov, G. Funka-Lea, Graph cuts and efficient N-D image segmentation, Int. J. Comput. Vis. 70 (2) (2006) 109–131, http://dx.doi.org/10.1007/s11263-006-7934-5.

[68] J. Shi, J. Malik, Normalized cuts and image segmentation, IEEE Trans. Pattern Anal. Mach. Intell. 22 (8) (2000) 888–905, http://dx.doi.org/10.1109/34.868688.

[69] Y. Boykov, V. Kolmogorov, An experimental comparison of min-cut/max-flow algorithms for energy minimization in vision, IEEE Trans. Pattern Anal. Mach. Intell. 26 (9) (2004) 1124–1137, http://dx.doi.org/10.1109/TPAMI.2004.60.

[70] C. Couprie, L. Grady, L. Najman, H. Talbot, Power watershed: A unifying graph-based optimization framework, IEEE Trans. Pattern Anal. Mach. Intell. 33 (7) (2011) 1384–1399, http://dx.doi.org/10.1109/TPAMI.2010.200.

[71] C. Harris, M. Stephens, A combined corner and edge detector, in: Proceedings of the 4th Alvey Vision Conference, 1988, pp. 147–151, http://dx.doi.org/10.5244/C.2.23.